

Document downloaded from the institutional repository of the University of
Alcala: <http://dspace.uah.es/dspace/>

This is a postprint version of the following published document:

Núñez-Cascajero, A., Valdueza-Felip, S., Monteagudo-Lerma, L., Monroy, E., Taylor-Shaw, E., Martin, R.W., González-Herráez, M., Naranjo, F.B., 2017, "In-rich AlxIn1-xN grown by RF-sputtering on sapphire: From closely-packed columnar to high-surface quality compact layers", Journal of Physics D: Applied Physics, 50 (6), art. n. 065101

Available at <http://dx.doi.org/10.1088/1361-6463/aa53d5>

Copyright 2017 IOP Publishing Ltd.

(Article begins on next page)



This work is licensed under a

Creative Commons Attribution-NonCommercial-NoDerivatives
4.0 International License.

In-rich $\text{Al}_x\text{In}_{1-x}\text{N}$ grown by RF-sputtering on sapphire: from closely-packed columnar to high-surface quality compact layers

A Núñez-Cascajero¹, S Valdueza-Felip^{2,3}, L Monteagudo-Lerma¹, E Monroy^{2,3},
E Taylor-Shaw⁴, R W Martin⁴, M González-Herráez¹ and F B Naranjo¹

¹*Grupo de Ingeniería Fotónica, Departamento de Electrónica, Universidad de Alcalá, Ctra. Madrid-Barcelona km. 33.6, 28871 Alcalá de Henares, Madrid, Spain*

²*Université Grenoble-Alpes, 38000, Grenoble, France*

³*CEA-Grenoble, INAC/PHELIQS, 17 av. des Martyrs, 38054 Grenoble, France*

⁴*Department of Physics, SUPA, University of Strathclyde, Glasgow, G4 0NG, United Kingdom*

E-mail: arantzazu.nunez@depeca.uah.es

The structural, morphological, electrical and optical properties of In-rich $\text{Al}_x\text{In}_{1-x}\text{N}$ ($0 < x < 0.39$) layers grown by reactive radio-frequency (RF) sputtering on sapphire are investigated as a function of the deposition parameters. The RF power applied to the aluminum target (0 W to 150 W) and substrate temperature (300 °C to 550 °C) are varied. X-ray diffraction measurements reveal that all samples have a wurtzite crystallographic structure oriented with *c*-axis along the growth direction. The aluminum composition is tuned by changing the power applied to the aluminum target while keeping the power applied to the indium target fixed at 40 W. When increasing the Al content from 0 to 0.39, the room-temperature optical band gap is observed to blue-shift from 1.76 eV to 2.0 eV, strongly influenced by the Burstein-Moss effect. Increasing the substrate temperature, results in an evolution of the morphology from closely-packed columnar to compact. For a substrate temperature of 500 °C and RF power for Al of 150 W, compact $\text{Al}_{0.39}\text{In}_{0.61}\text{N}$ films with a smooth surface (root-mean-square surface roughness below 1 nm) are produced.

Keywords: III-nitrides, AlInN, RF-sputtering, characterization, semiconductor...

1. Introduction

The III-nitride semiconductors AlN, GaN, InN and their ternary alloys have become increasingly important in applications such as light-emitting diodes [1], laser diodes [2], solar cells [3], high electron mobility transistors [4] and Bragg reflectors [5]. The ternary alloy $\text{Al}_x\text{In}_{1-x}\text{N}$ is of particular interest due to the wide-range of direct band gaps it presents, ranging from the near infrared (InN: 0.7 eV [6]) to the deep ultraviolet (AlN: 6.2 eV [7]), and its lattice match to GaN near $x=0.83$ [8]. These capabilities allow the design of a wide range of functional structures for many final applications, including UV emitters, high reflectivity mirrors and transistors for high temperature operation. However, the growth of high-quality and single-phase AlInN remains challenging due to the large immiscibility gap of the alloy [9,10] and the large growth temperature difference between InN and AlN [11].

There are a number of reports of the synthesis of AlInN layers using metal-organic chemical vapor deposition (MOVPE) [12,13] and molecular beam epitaxy (MBE) [14,15] as well as by sputtering deposition [16–27]. Sputtering deposition allows low temperature deposition thanks to the high kinetic energy of the ions involved in the growth process. It also permits the deposition of polycrystalline films on large area substrates using a low cost process, but at the expense of delivering layers with lower crystal quality than those grown by MOVPE or MBE. The use of sputtering to deposit AlInN on a wide range of substrates, including sapphire, silicon, and quartz, and at different deposition temperatures has been reported by a number of groups [16–27]. A mixture of argon and nitrogen is usually used for the plasma generation. In this report we study the optimization of the deposition conditions for AlInN on sapphire substrates under pure nitrogen plasma. The use of pure nitrogen instead of an argon and nitrogen mixture leads to lower deposition rates and thus the layer properties are highly affected.

We have previously reported a study of AlInN sputtered films on Si(111) substrates using pure nitrogen [27] showing that the growth temperature does not affect significantly to the morphological properties of the layers. In this work, we investigate the effect of varying the power applied to the

aluminum target (0 W to 150 W) and the substrate temperature (300 °C to 550 °C) on the properties of high In-content $\text{Al}_x\text{In}_{1-x}\text{N}$ grown by reactive radio-frequency (RF) magnetron sputtering on *c*-sapphire substrates. We demonstrate that the growth kinetics, the Al content ($0 < x < 0.39$) and the layer morphology (ranging from closely-packed nanocolumns to compact) of the layers can be controlled through these two parameters. The optical band gap as a function of Al composition and the resultant bowing parameter are estimated.

2. Experimental methods

A reactive RF-sputtering system (AJA International, ATC ORION-3-HV) was used to deposit $\text{Al}_x\text{In}_{1-x}\text{N}$ samples on (0001)-oriented sapphire substrates. This sputtering system is equipped with three 2-inch confocal magnetron guns. The ternary deposition was carried out by simultaneously sputtering from separate targets of pure In (99.995 %) and pure Al (99.999 %), with pure nitrogen (99.9999 %) used as the reactive gas. The substrate-target distance was fixed at 10.5 cm. A thermocouple placed in direct contact with the substrate holder is used to monitor the substrate temperature during deposition. The substrates were chemically cleaned in organic solvents before being loaded in the sputtering chamber where they were outgassed for 30 min at 550 °C. After this cleaning procedure, the substrates were cooled down to the growth temperature. Prior to the deposition, the targets and the substrate were cleaned using plasma etching with Ar (99.999 %) in the growth chamber. $\text{Al}_x\text{In}_{1-x}\text{N}$ layers were then deposited with the nitrogen flow, sputtering pressure and RF power applied to the indium target kept at 14 sccm, 0.47 Pa and 40 W, respectively. A sputtering time of 4 h was used for all the samples.

Two sets of samples were prepared in order to study the influence of the deposition conditions on the properties of AlInN -on-sapphire layers. Firstly, the RF power applied to the Al target (P_{Al}) was varied from 0 W to 150 W with the substrate temperature (T_s) kept constant at 300 °C (set A, S1 — S5). Secondly, T_s was varied from 300 °C to 550 °C with P_{Al} fixed at 150 W (set B, S5 — S9).

Table 1: Summary of the structural and optical characterization results of the $\text{Al}_x\text{In}_{1-x}\text{N}$ samples: RF power applied to the Al target (P_{Al}); substrate temperature (T_s); thickness estimated with FESEM;

room-temperature absorption edge (E_g); absorption band edge broadening (ΔE); and room-temperature PL emission energy (E_{PL}).

Sample	P_{Al} (W)	T_s (°C)	Thickness (nm)	E_g (eV)	ΔE (meV)	E_{PL} (eV)
S1	0	300	365	1.76	143	1.59
S2	75	300	370	1.85	144	-
S3	85	300	370	1.88	145	1.71
S4	105	300	385	1.94	150	-
S5	150	300	530	2.03	154	1.86
S6	150	350	500	2.04	180	-
S7	150	450	575	1.98	210	-
S8	150	500	475	1.99	210	-
S9	150	550	455	2.00	220	1.65

The crystalline orientation, composition and mosaicity of the deposited films were estimated from high-resolution X-ray diffraction (HRXRD) measurements obtained using a four-axis Bruker AXS D8 Advance diffractometer. The composition was also measured by wavelength dispersive X-ray (WDX) spectroscopy using a Cameca SX100 electron probe micro-analyzer (EPMA), with a 7 kV electron beam which probes the topmost ~ 200 nm of the layer [28]. Atomic force microscopy (AFM) was employed to characterize the surface morphology, using a Veeco Dimension 3100 microscope in tapping mode, with WSxM software [29] used for data processing and image generation. A Zeiss Ultra 55 field-emission scanning electron microscope (FESEM) was used to characterize the morphology and to estimate the thicknesses of the layers. The electrical properties of the layers were analyzed using room temperature Hall-effect measurements and a conventional Van der Pauw geometry. The optical properties of the layers were estimated from transmittance measurements performed at normal incidence over a 350–1700 nm wavelength range using an optical spectrum analyzer and

photoluminescence (PL) data excited using a 23 mW laser diode. The PL was dispersed by a 45 cm focal-length Jobin-Yvon monochromator coupled to a charge-coupled-device (CCD) camera for detection.

3. Results and discussion

3.1. Structural and morphological characterization

Figure 1 depicts the $2\theta/\omega$ X-ray scans obtained by HRXRD corresponding to the RF power (P_{Al}) series of samples in set A. The two peaks observed within the 2θ analyzed span correspond to the $\text{Al}_x\text{In}_{1-x}\text{N}$ (0002) and the Al_2O_3 (0006) reflections, confirming the wurtzite structure of the layers with the c -axis aligned to that of the sapphire substrate. Increasing P_{Al} leads to an increase of the diffraction angle for the $\text{Al}_x\text{In}_{1-x}\text{N}$ layer reflection, corresponding to a reduction of the c lattice parameter from 5.741 Å for S1 to 5.474 Å for S5. The Al content of the layers, estimated assuming they are fully relaxed by applying Vegard's law [30] and considering the lattice parameters of InN ($c_{\text{InN}} = 5.703$ Å) and AlN ($c_{\text{AlN}} = 4.982$ Å) [31], increases from 0 to 0.32 as a function of P_{Al} for the studied range (samples S1 to S5 in Table 2). In the case of the samples grown ranging the substrate temperature, only the peak related to AlInN (0002) diffraction is observed (not shown), which barely changes its position with the growth temperature (see table 2).

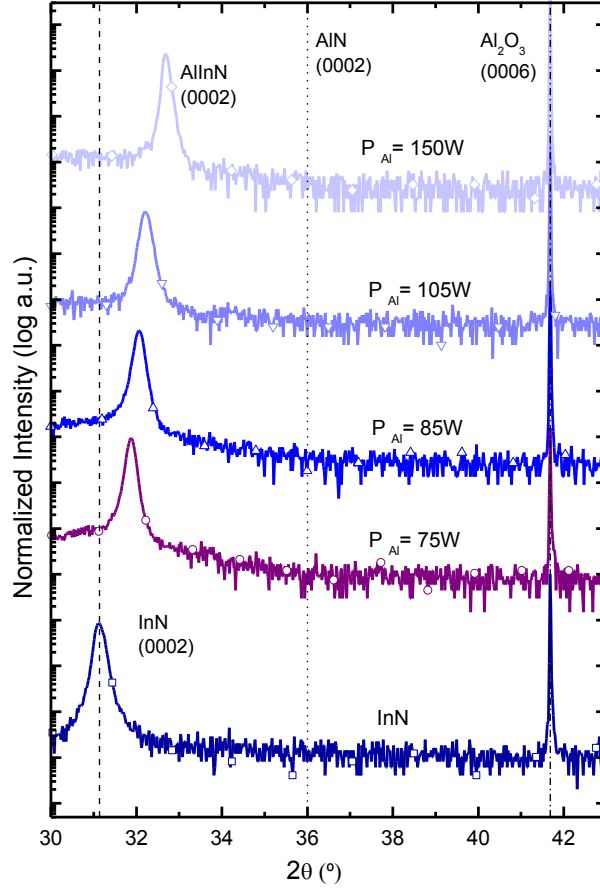


Figure 1: $2\theta/\omega$ scans of the samples of set A. The dash line shows the position of the InN (0002) reflection peak while the dotted line shows the position of the AlN (0002) reflection peak.

The Al composition of the layers was further investigated by WDX measurements, obtaining values slightly higher than those calculated from HRXRD. This difference is attributed to residual strain present in the layers due to the lattice mismatch with the sapphire substrate (22.5% and 11.7% in-plane lattice mismatch for InN and AlN on sapphire, respectively). To estimate the strain state (ε_{zz}) of the $\text{Al}_x\text{In}_{1-x}\text{N}$ layers, the relaxed lattice parameter c has been calculated using the Al mole fraction extracted from WDX measurements (c_{WDX}). Then, the strain along the c -axis has been calculated as $\varepsilon_{zz} = (c_{HRXRD} - c_{WDX})/c_{WDX}$, obtaining values in the $(0.9 \text{ to } 5.3) \times 10^{-3}$ range (tensile strain). Assuming that the stress during the growth was biaxial, i.e. isotropic in-plane stress and no stress along the growth axis, the in-plane strain can be calculated as $\varepsilon_{xx} = -\varepsilon_{zz}c_{33}/2c_{13}$, where c_{13} and c_{33} are elastic constants. Assuming $c_{13} = 92 \text{ GPa}$ and $c_{33} = 224 \text{ GPa}$ for InN and $c_{13} = 108 \text{ GPa}$ and $c_{33} = 373 \text{ GPa}$ for AlN [31], ε_{xx} is in the range of $(-1.2 \text{ to } -7.6) \times 10^{-3}$ (compressive strain). The

compressive nature of ϵ_{xx} is consistent with the growth on sapphire substrates, and the fact that the layers are almost fully relaxed is expected in such a mismatched heteroepitaxial system (see Table 2). It should be pointed out that the value of $|\epsilon_{zz}|$ increases when increasing the layer thickness (see tables 1 and 2), which points to the aluminum content as the main factor at the origin of the strain state of the layers. Furthermore, three layers (S5, S7 and S9) with similar Al composition and different thickness present similar strain state.

Table 2: Summary of the Al mole fraction x and c -axis parameter extracted from HRXRD and WDX measurements respectively; strain along the (0001) axis (ϵ_{zz}); in-plane strain (ϵ_{xx}).

Sample	P_{Al} (W)	T_s (°C)	x_{HRXRD}	c_{HRXRD} (Å)	x_{WDX}	c_{WDX} (Å)	ϵ_{zz} (%)	ϵ_{xx} (%)
S1	0	300	0	5.741	-	-	-	-
S2	75	300	0.13	5.611	-	-	-	-
S3	85	300	0.17	5.579	0.18	5.574	0.09	-0.12
S4	105	300	0.21	5.553	0.24	5.531	0.40	-0.54
S5	150	300	0.32	5.474	0.36	5.445	0.53	-0.76
S6	150	350	0.34	5.455	-	-	-	-
S7	150	450	0.33	5.465	0.38	5.431	0.63	-0.90
S8	150	500	0.35	5.452	-	-	-	-
S9	150	550	0.35	5.453	0.39	5.423	0.55	-0.78

The AlInN films (S2–S5) present a FWHM of the ω -scan of the (0002) reflection in the range of 1.4°–1.9°, without a clear trend as a function of P_{Al} . These values are comparable with previous results in AlInN samples grown by MBE [32].

The evolution of the root-mean-square (rms) surface roughness of the AlInN films with P_{Al} is shown in figure 2(a), with measurements being extracted from $2 \times 2 \mu\text{m}^2$ AFM images. The surface roughness increases markedly when incorporating Al to the InN layer due to the change in the layer morphology

from a compact InN layer (S1) to a closely-packed columnar $\text{Al}_{0.13}\text{In}_{0.87}\text{N}$ structure (S2). See figure 2 (b-e) that shows the AFM micrographs and cross-sectional FESEM images of the InN sample (S1) and the AlInN sample deposited with $P_{\text{Al}} = 75 \text{ W}$ (S2) for clarity. This change is explained by the low mobility of the impinging Al atoms which leads to a reduction of the capability for surface diffusion of In and N species. Further increase of the P_{Al} from 75 W to 150 W, induces an increase of the Al incorporation into the layer (see Table 2) and a decrease of the surface roughness while keeping the closely-packed columnar morphology unaltered (see AFM and FESEM images of S5 in figures 3(b) and 3(c), respectively). This surface roughness reduction for increasing P_{Al} is attributed to the increased kinetic energy of the Al atoms impinging the growing surface.

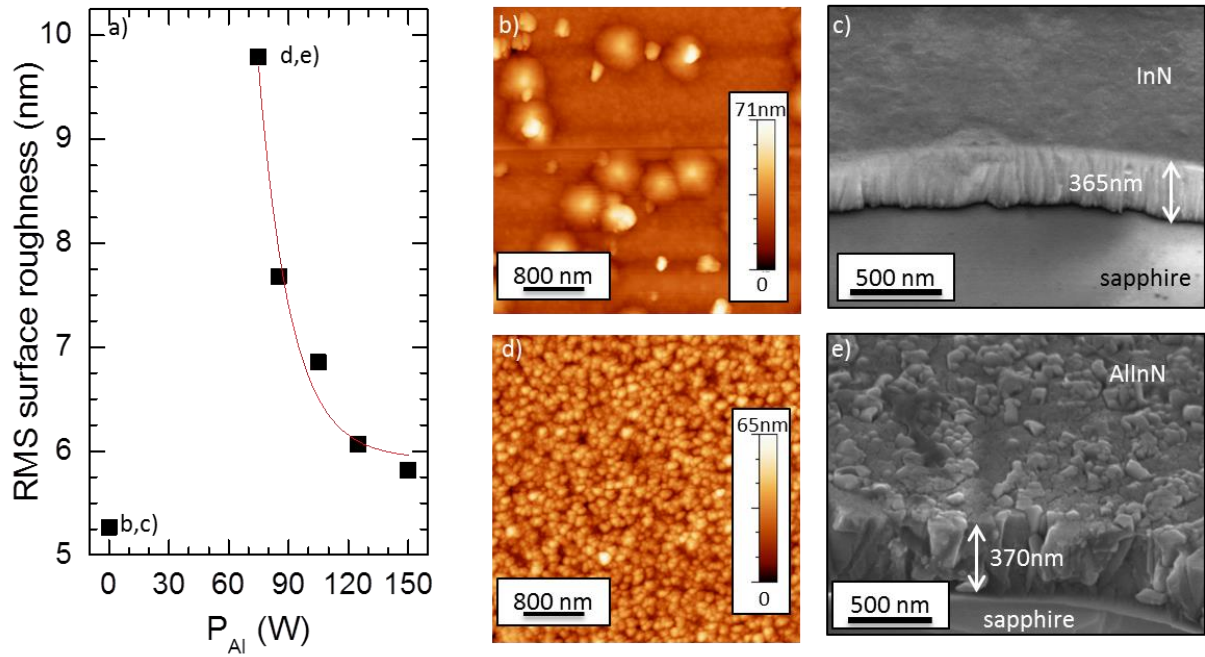


Figure 2: a) Rms surface roughness evolution of the $\text{Al}_x\text{In}_{1-x}\text{N}$ samples as a function of P_{Al} . The solid line is a guide to the eye. b) 4x4 μm^2 AFM and c) SEM of the InN layer (S1, $P_{\text{Al}} = 0$); d) 4x4 μm^2 AFM and e) SEM of the $\text{Al}_{0.13}\text{In}_{0.87}\text{N}$ layer (S2, $P_{\text{Al}} = 75 \text{ W}$). The AFM and SEM images of the sample grown at P_{Al} of 150 W (S5) are shown in figure 3 (b) and 3 (c).

The mobility of the adsorbed species can be improved by increasing the substrate temperature, which should therefore compensate the presence of Al. This effect is studied with the second sample set (set

B, samples S5-S9) where the substrate temperature was varied from $T_s = 300\text{ }^\circ\text{C}$ to $550\text{ }^\circ\text{C}$ and P_{Al} was held constant at 150 W. WDX measurements indicate a slight increase of the Al mole fraction in the layers as a function of the substrate temperature, from 0.36 to 0.39 in the range under study. The compositional change is consistent with an enhanced desorption of physi-adsorbed In atoms.

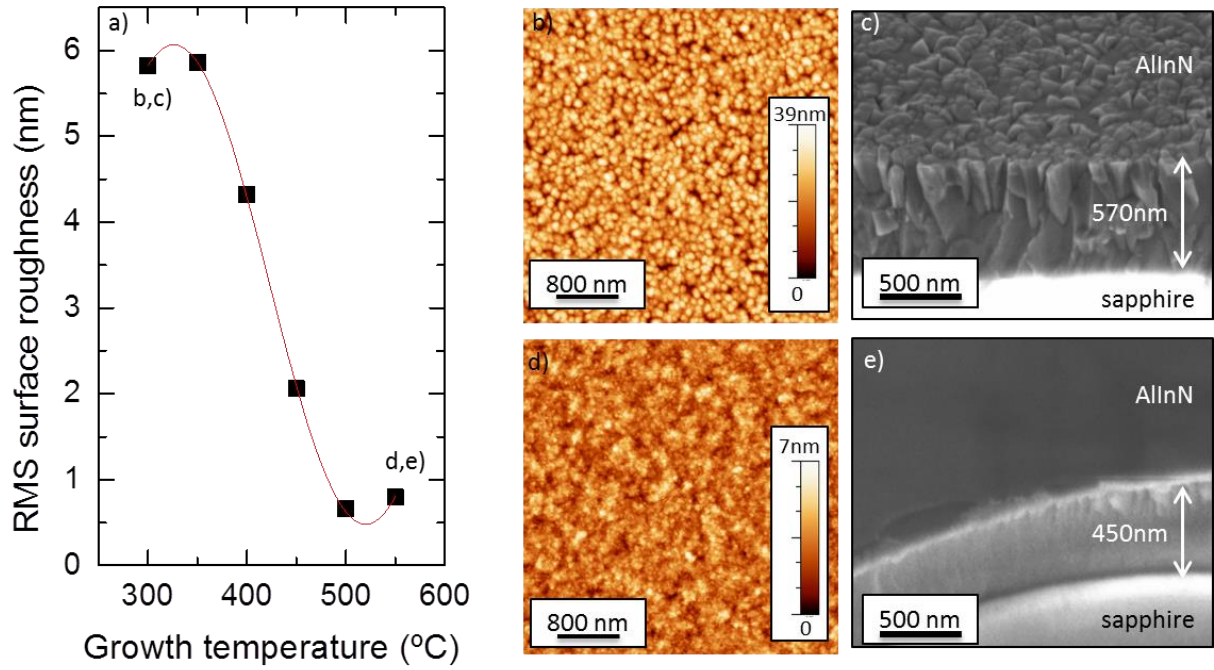


Figure 3: a) Estimated rms surface roughness of $\text{Al}_x\text{In}_{1-x}\text{N}$ samples as a function of T_s with P_{Al} of 150 W. The solid line is a guide to the eye. b) $4 \times 4\text{ }\mu\text{m}^2$ AFM and c) SEM of the AlInN layer grown at $300\text{ }^\circ\text{C}$ (S5); d) $4 \times 4\text{ }\mu\text{m}^2$ AFM and e) SEM of the AlInN layer grown at $550\text{ }^\circ\text{C}$ (S9).

A gradual change in morphology occurs when increasing the growth temperature as shown in figures 3(b, c) and 3(d, e) for samples S5 ($300\text{ }^\circ\text{C}$) and S9 ($550\text{ }^\circ\text{C}$), respectively. When increasing the substrate temperature, the layers evolve from closely-packed columnar structures to compact films, with a reduction of the growth rate from 143 nm/h to 113 nm/h . This indicates that the higher substrate temperature compensates the drop in kinetic energy caused by the presence of Al. Furthermore, the rms surface roughness drops from 5.8 nm to 0.8 nm (comparable to best values for sputtered AlN on sapphire [33]) when the growth temperature increases from $300\text{ }^\circ\text{C}$ to $550\text{ }^\circ\text{C}$, as illustrated in figure

3(a).

3.2. Electrical characterization

Figure 4 shows the room temperature resistivity and the free carrier concentration of the $\text{Al}_x\text{In}_{1-x}\text{N}$ layers as a function of (a) the Al mole fraction extracted from WDX, except in the case of S2 where it is extracted from XRD (in this case the Al mole fraction measured by XRD and WDX should be comparable because, as observed in Table 1, the differences between these measurements increases when increasing the Al composition (set A) or the substrate temperature (set B)). In set A (S1–S5), increasing the Al composition from $x = 0$ to 0.36 causes the carrier concentration to drop by more than one order of magnitude and the resistivity to increase from $\rho_s = 0.2 \text{ m}\Omega\cdot\text{cm}$ to $11.5 \text{ m}\Omega\cdot\text{cm}$. The results for InN are in agreement with previous literature [34,35]. Several factors might contribute to the observed change in electrical properties of the $\text{Al}_{0.13}\text{In}_{0.87}\text{N}$ layer in comparison to those of the InN. On the one hand, the columnar morphology results in an increase of the resistivity and a decrease in the carrier concentration due to scattering, carrier trapping and band bending at the boundaries. On the other hand, the widening of the band gap by Al incorporation should lead to an increase of the activation energy of the impurities and a decrease of the carrier concentration, giving a trend that is also observed when increasing the Al content [36].

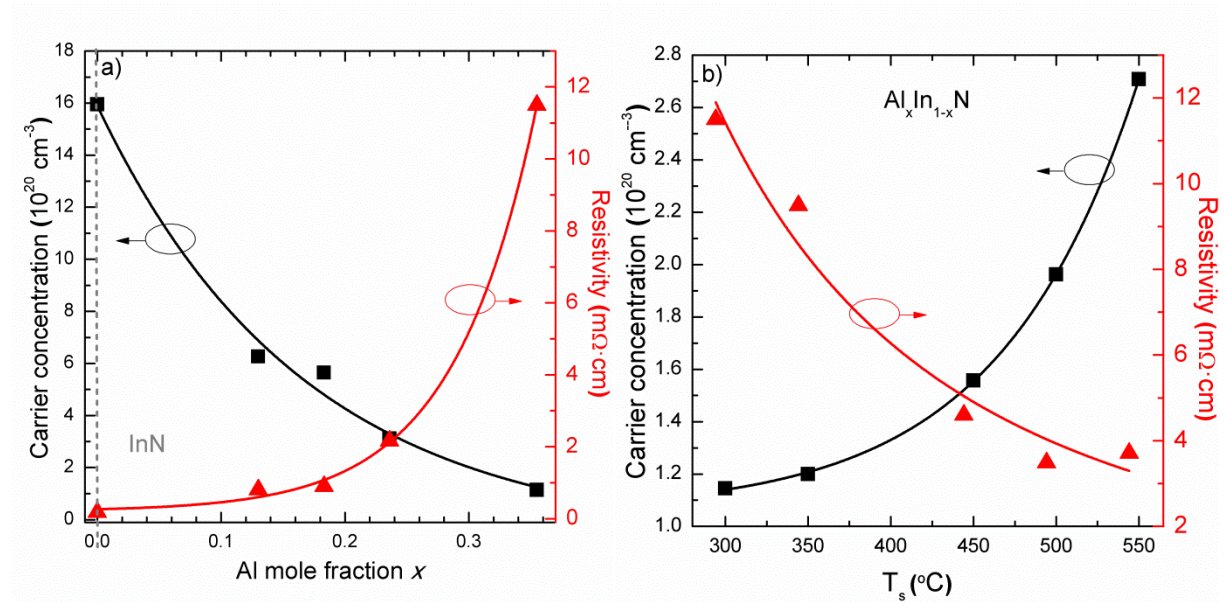


Figure 4: Dependence of the AlInN carrier concentration and resistivity on: a) the aluminum mole fraction and b) the substrate temperature.

In set B (S5–S9), the increase of the mobility of the adatoms on the surface when increasing substrate temperature does not have any remarkable effect on the Al content of the layer, but it does significantly change the deposition mode. This increase in the adatom mobility and thus the change in the morphology from closely-packed nanocolumns (S5) to a compact layer (S9) leads to a drop of the resistivity from $\rho_s = 11.5 \text{ m}\Omega\cdot\text{cm}$ to $3.7 \text{ m}\Omega\cdot\text{cm}$, which confirms that the enhancement observed in this set was indeed due to the morphology. During the growth of thin films different steps happen, namely the nucleation of small islands, then the growth and coalescence of the islands, and finally the two-dimensional growth [37]. The process of attaining two-dimensional growth relies on a high enough adatom mobility, which depends on the growth conditions and on the nature of the substrate. In this particular case, an enhancement of the adatom mobility is achieved by increasing the substrate temperature. The resistivity drop is also associated with an increase of the carrier concentration, but only by a factor of 2. For the compact $\text{Al}_{0.39}\text{In}_{0.61}\text{N}$ sample, S9, the values of resistivity and mobility ($\rho_s = 3.7 \text{ m}\Omega\cdot\text{cm}$ and $\mu \cong 6.2 \text{ cm}^2/\text{Vs}$) are similar to those reported by Liu *et al.* ($\rho_s = 1.2 \text{ m}\Omega\cdot\text{cm}$ and $\mu = 11.4 \text{ cm}^2/\text{Vs}$ for $\text{Al}_{0.28}\text{In}_{0.72}\text{N}$ layers [38]).

3.3. Optical properties

The inset of figure 5(a) shows the transmission spectra of several samples in set A. The absorption of the samples is estimated from transmission spectra considering the relation $\alpha(E) \propto -\ln(\text{Tr})$, which neglects optical scattering and reflection losses. The apparent optical band gap energy (E_g) is then obtained through a linear fit of the squared absorption coefficient as a function of the photon energy (dashed line in figure 5(a)). The room-temperature values of E_g are summarized in Table 1 and show a blue-shift from $E_g = 1.76 \text{ eV}$ ($\lambda_g = 704 \text{ nm}$) for InN (S1) to $E_g \sim 2.0 \text{ eV}$ ($\lambda_g = 610 \text{ nm}$) for $\text{Al}_{0.39}\text{In}_{0.61}\text{N}$ (S9). These values of E_g are related to the high carrier concentration measured in the layers and the Burstein-Moss effect.

The absorption spectrum of the layers was modeled by using a sigmoidal approximation, given by:

$$\alpha = \frac{\alpha_0}{1 + e^{\frac{E_0 - E}{\Delta E}}} \quad (1)$$

where α_0 is the above band-gap absorption, ΔE the absorption edge broadening of the samples, E is the photon energy, and E_0 is a fitting parameter that marks the inflection point of the sigmoidal function [39]. An average value of $\alpha_0 = (1.1 \pm 0.2) \times 10^5 \text{ cm}^{-1}$ is obtained, with ΔE increasing from 143 meV to 220 meV with the Al incorporation, as summarized in Table 1.

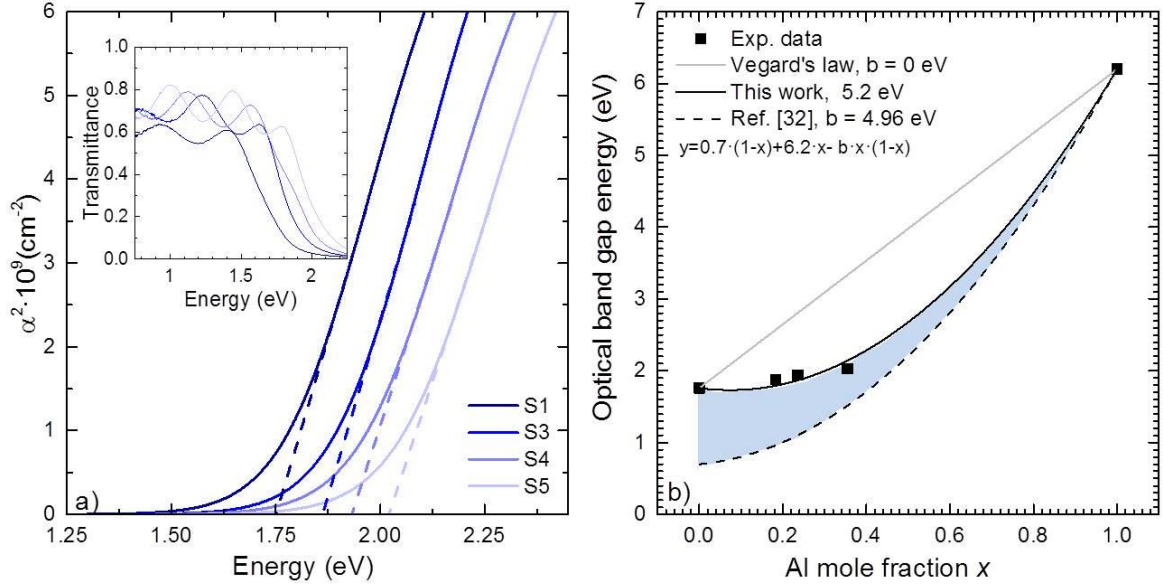


Figure 5: a) Square of the absorption coefficient as a function of the photon energy of $\text{Al}_x\text{In}_{1-x}\text{N}$ layers with different composition. The inset shows the room-temperature transmittance spectra of the same layers. b) The band gap energy of $\text{Al}_x\text{In}_{1-x}\text{N}$ as a function of Al composition (from WDX), including a parabolic guide to the eye and an indication (shaded) of the difference from a bowing parameter expression using the band-gap of pure InN.

Figure 5(b) depicts E_g as a function of the Al composition extracted from WDX (x) also including a comparison of our data with experimental results in $\text{Al}_x\text{In}_{1-x}\text{N}$ layers grown by MBE [32]. The difference between both curves is explained by the Burstein-Moss effect due to the high carrier concentration of samples grown by sputtering. This difference decreases for AlInN when increasing the aluminum content because of the measured reduction of carrier concentration with the Al content (blue shadow in figure 5(b) as a guide to the reader).

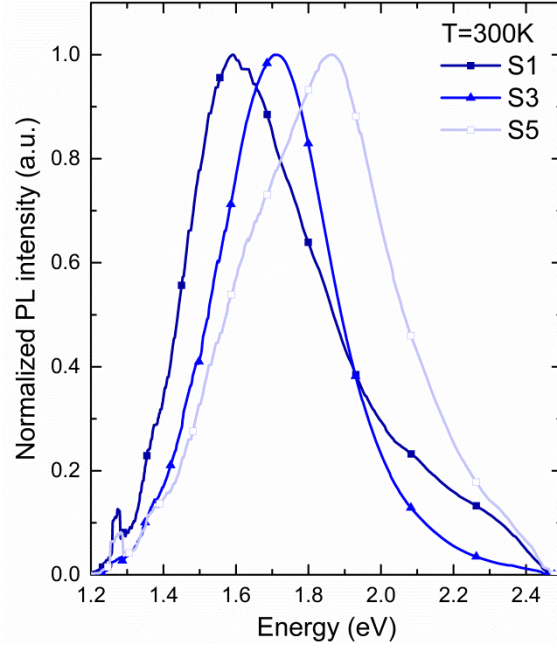


Figure 6: Normalized room-temperature PL emission spectra of the samples grown with different P_{Al} . The peak that appears at ~ 1.3 eV is an artifact of the PL setup.

The room-temperature PL emission of samples of set A is shown in figure 6, a FWHM in the 370 – 490 meV range is measured. The Stokes shift (difference between the PL emission and the absorption edge energies) is ~ 170 meV for all the samples of set A, similar to results reported by other authors for sputtered InN films [40]. However, in series B, the Stokes shift increases from ~ 170 meV for S5 to ~ 350 meV for S9. This difference might be related to the higher alloy inhomogeneity while the layers gain in compactness, probably associated to the higher deposition temperature. This high Stokes shift is in agreement with the calculations of Jiang *et al.* [18] who relate it with fluctuations in the In distribution, or with deep defects or impurities acting as preferential recombination centers. It should be pointed out that the PL peak emission energy of the sample S9 recovers the value obtained for the InN sample (1.65 eV versus 1.59 eV, as summarized in Table 1).

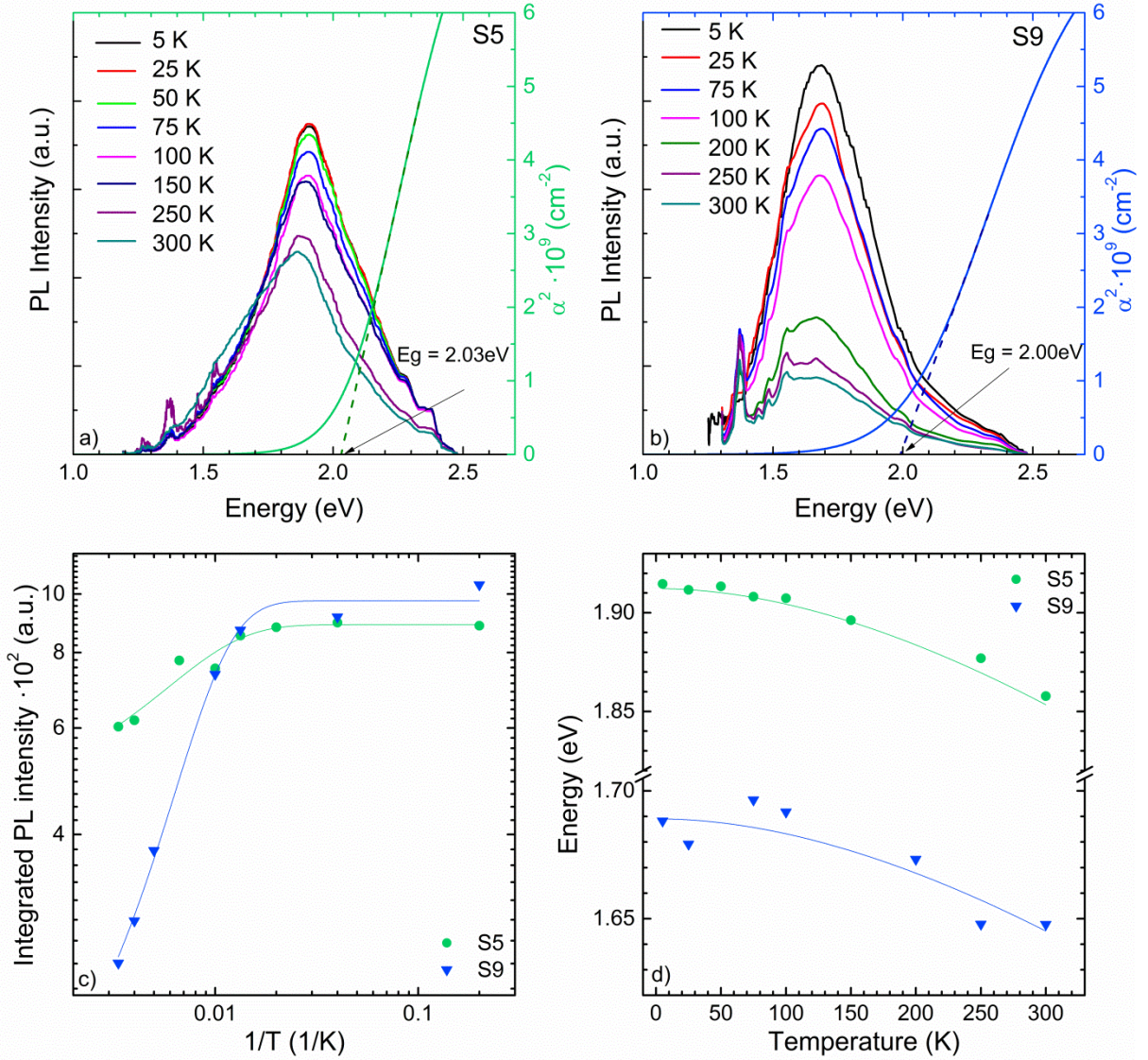


Figure 7: Temperature-dependent PL spectra of a) $\text{Al}_{0.36}\text{In}_{0.64}\text{N}$ (S5) and b) $\text{Al}_{0.39}\text{In}_{0.61}\text{N}$ (S9). c) Thermal evolution of the integrated PL emission intensity of the analyzed $\text{Al}_x\text{In}_{1-x}\text{N}$ layers. The solid lines show the fit of the experimental data to equation (2). d) Temperature dependence of the PL emission peak energy. The solid lines indicate the agreement of the experimental data to Varshni's equation, (3). The peak that appears at $\sim 1.3\text{ eV}$ is an artifact of the PL setup.

The evolution of the PL emission with temperature was investigated in the temperature range of $T = 5\text{ K}$ to 300 K , as shown in figure 7(a) and (b) for samples S5 (columnar) and S9 (compact), respectively. Figure 7(c) shows the integrated PL emission as a function of temperature. The thermal evolution of the PL is characterized by a quenching of the intensity due to the activation of

nonradiative recombination processes, together with a red shift and broadening of the emission. The PL intensity of the columnar $\text{Al}_{0.36}\text{In}_{0.64}\text{N}$ sample (S5) drops by a factor of approximately x1.6 from $T = 5$ K to room-temperature, whereas it drops by x5 for the compact $\text{Al}_{0.39}\text{In}_{0.61}\text{N}$ sample (S9). In both cases, the evolution of the PL emission integrated intensity, $I(T)$, follows the equation (2), which considers a single nonradiative recombination channel [41]:

$$I(T) = \frac{I_0}{1 + a \cdot e^{\frac{E_a}{k_B T}}} \quad (2)$$

In equation (2), I_0 is the integrated intensity at 0 K, E_a represents the activation energy of the quenching process, $k_B T$ is the thermal energy, and a is a fitting constant related to a nonradiative-to-radiative recombination ratio of the extinction process [41]. The fits of the experimental data with equation (2) are displayed by solid lines in figure 7(c). Values of activation energy of $E_a = 19 \pm 7$ meV and $E_a = 28 \pm 5$ meV are obtained for S5 and S9 samples, respectively. The values of a vary from 0.96 to 8.6, for S5 and S9, respectively.

The Varshni [42] equation (3) was used describe the evolution of the PL peak emission energy with the temperature.

$$E_{\text{PL}}(T) = E_{\text{PL}}(0) - \frac{\gamma T^2}{\beta + T} \quad (3)$$

Equation (3) involves the PL emission energy at 0 K $E_{\text{PL}}(0)$, and two fitting constants, γ and β . These fitting constants are obtained taking into account the γ and β of the binary compounds [31]. Considering the composition of the AlInN layers, and applying the Vegard's law, values of $\gamma = 0.74$ meV/K and $\beta = 890$ K for S5, and $\gamma = 0.8$ meV/K and $\beta = 920$ K for S9, are obtained. Figure 7(d) shows the evolution of the PL emission energy for S5 and S9 samples with temperature, in which the solid lines show the agreement of the experimental data to equation (3).

4. Conclusions

In conclusion, we have studied the influence of growth parameters (power applied to the aluminum target and substrate temperature) on the properties of $\text{Al}_x\text{In}_{1-x}\text{N}$ layers grown on (0001)-oriented

In-rich $\text{Al}_x\text{In}_{1-x}\text{N}$ grown by RF-sputtering on sapphire

sapphire substrates by reactive RF-sputtering. The power applied to the aluminum target controls the composition of the alloy, while the surface morphology evolves from columnar to compact layers when varying the substrate temperature while keeping constant the Al content. For the analyzed growth conditions, samples grown over 500 °C and at 150 W of P_{Al} ($x=0.39$) attain the best properties, i.e. compact morphology with high surface quality (roughness below 1 nm) and a band gap energy of 2 eV, making them appropriate for their application to photoconductors and high reflectivity mirrors in the visible wavelength range.

Acknowledgements

This work was partially supported by the projects TEC2015-71127-C2-2-R (Spanish Government), S2013/MIT 2790 (Community of Madrid), CCG2015/EXP-014 (University of Alcalá) and the FPI Grant from the University of Alcalá, and by the Marie Curie IEF grant “SolarIn” (#331745). Authors acknowledge the X-ray Diffraction Techniques Laboratory at the ICMM-CSIC for X-ray diffraction measurements.

References

- [1] Weisbuch C, Piccardo M, Martinelli L, Iveland J, Peretti J and Speck J S 2015 The efficiency challenge of nitride light-emitting diodes for lighting *Physica Status Solidi (a)* **212** 899–913
- [2] Muziol G, Siekacz M, Turski H, Wolny P, Grzanka S, Grzanka E, Feduniewicz-Żmuda A, Borysiuk J, Sobczak K, Domagała J, Nowakowska-Siwińska A, Makarowa I, Perlin P and Skierbiszewski C 2015 High power nitride laser diodes grown by plasma assisted molecular beam epitaxy *Journal of Crystal Growth* **425** 398–400
- [3] Yamamoto A, Islam M R, Kang T T and Hashimoto A 2010 Recent advances in InN-based solar cells: Status and challenges in InGaN and InAlN solar cells *Physica Status Solidi (C)* **7** 1309–16
- [4] Espinosa N, Schwarz S U, Cimalla V and Ambacher O 2015 Detection of different target-DNA concentrations with highly sensitive AlGaIn/GaN high electron mobility transistors *Sensors and Actuators B: Chemical* **210** 633–9
- [5] Berger C, Dadgar A, Bläsing J, Lesnik A, Veit P, Schmidt G, Hempel T, Christen J, Krost A and Strittmatter A 2015 Growth of AlInN/GaN distributed Bragg reflectors with improved interface quality *Journal of Crystal Growth* **414** 105–9
- [6] Wu J, Walukiewicz W, Yu K M, Ager J W, Haller E E, Lu H, Schaff W J, Saito Y and Nanishi Y 2002 Unusual properties of the fundamental band gap of InN *Applied Physics Letters* **80** 3967–9
- [7] Yim W M, Stofko E J, Zanzucchi P J, Pankove J I, Ettenberg M and Gilbert S L 1973 Epitaxially grown AlN and its optical band gap *Journal of Applied Physics* **44** 292–6
- [8] Lorenz K, Franco N, Alves E, Watson I M, Martin R W and O'Donnell K P 2006 Anomalous ion channeling in AlInN/GaN bilayers: Determination of the strain state *Physical Review Letters* **97** 1–4
- [9] Hums C, Bläsing J, Dadgar A, Diez A, Hempel T, Christen J, Krost A, Lorenz K and Alves E 2007 Metal-organic vapor phase epitaxy and properties of AlInN in the whole compositional range *Applied Physics Letters* **90** 22105
- [10] Ferhat M and Bechstedt F 2002 First-principles calculations of gap bowing in $\text{In}_x\text{Ga}_{1-x}\text{N}$ and $\text{In}_x\text{Al}_{1-x}\text{N}$ alloys: Relation to structural and thermodynamic properties *Physical Review B* **65** 75213
- [11] Neumayer D A and Ekerdt J G 1996 Growth of Group III Nitrides. A Review of Precursors and Techniques *Chemistry of Materials* **8** 9–25
- [12] Yamaguchi S, Kariya M, Nitta S, Kato H, Takeuchi T, Wetzel C, Amano H and Akasaki I 1998 Structural and optical properties of AlInN and AlGaInN on GaN grown by metalorganic vapor phase epitaxy *Journal of Crystal Growth* **195** 309–13
- [13] Aschenbrenner T, Dartsch H, Kruse C, Anastasescu M, Stoica M, Gartner M, Pretorius A, Rosenauer A, Wagner T and Hommel D 2010 Optical and structural characterization of AlInN layers for optoelectronic applications *Journal of Applied Physics* **108** 63533
- [14] Chen W C, Wu Y H, Peng C Y, Hsiao C N and Chang L 2014 Effect of In/Al ratios on structural and optical properties of InAlN films grown on Si(100) by RF-MOMBE *Nanoscale Research Letters* **9** 1–7
- [15] Wu Y H, Wong Y Y, Chen W C, Tsai D S, Peng C Y, Tian J S, Chang L and Yi Chang E 2014 Indium-rich InAlN films on GaN/sapphire by molecular beam epitaxy *Materials Research Express* **1** 15904
- [16] Guo Q, Tanaka T, Nishio M and Ogawa H 2008 Structural and Optical Properties of AlInN Films Grown on Sapphire Substrates *Japanese Journal of Applied Physics* **47** 612
- [17] Dong C J, Xu M, Chen Q Y, Liu F S, Zhou H P, Wei Y and Ji H X 2009 Growth of well-

- oriented $\text{Al}_x\text{In}_{1-x}\text{N}$ films by sputtering at low temperature *Journal of Alloys and Compounds* **479** 812–5
- [18] Jiang L F, Shen W Z and Guo Q X 2009 Temperature dependence of the optical properties of AlInN *Journal of Applied Physics* **106** 13515
- [19] He H, Cao Y, Fu R, Guo W, Huang Z, Wang M, Huang C, Huang J and Wang H 2010 Band gap energy and bowing parameter of In-rich InAlN films grown by magnetron sputtering *Applied Surface Science* **256** 1812–6
- [20] He H, Cao Y, Fu R, Wang H, Huang J, Huang C, Wang M and Deng Z 2010 Structure and optical properties of InN and InAlN films grown by rf magnetron sputtering *Journal of Materials Science: Materials in Electronics* **21** 676–81
- [21] Lü M, Dong C and Wang Y 2013 Proposal and achievement of a relatively Al-rich interlayer for In-rich $\text{Al}_x\text{In}_{1-x}\text{N}$ films deposition *Journal of Wuhan University of Technology-Mater. Sci. Ed.* **28** 868–75
- [22] Liu H F, Dolmanan S B, Tripathy S, Dalapati G K, Tan C C and Chi D Z 2013 Effects of AlN thickness on structural and transport properties of In-rich $n\text{-AlInN}/\text{AlN}/\text{p-Si}(001)$ heterojunctions grown by magnetron sputtering *Journal of Physics D: Applied Physics* **46** 95106
- [23] Kubota K, Kobayashi Y and Fujimoto K 1989 Preparation and properties of III-V nitride thin films *Journal of Applied Physics* **66** 2984–8
- [24] Peng T, Piprek J, Qiu G, Olowolafe J O, Unruh K M, Swann C P and Schubert E F 1997 Band gap bowing and refractive index spectra of polycrystalline $\text{Al}_x\text{In}_{1-x}\text{N}$ films deposited by sputtering *Applied Physics Letters* **71** 2439–41
- [25] Guo Q X, Okazaki Y, Kume Y, Tanaka T, Nishio M and Ogawa H 2007 Reactive sputter deposition of AlInN thin films *Journal of Crystal Growth* **300** 151–4
- [26] Guo Q, Yahata K, Tanaka T, Nishio M and Ogawa H 2003 Growth and characterization of reactive sputtered AlInN films *Physica Status Solidi (C)* **0** 2533–6
- [27] Núñez-Cascajero A, Monteagudo-Lerma L, Valdueza-Felip S, Navío C, Monroy E, González-Herráez M and Naranjo F B 2016 Study of high In-content AlInN deposition on $\text{p-Si}(111)$ by RF-sputtering *Japanese Journal of Applied Physics* **55**05FB07
- [28] Taylor E, Smith M D, Sadler T C, Lorenz K, Li H N, Alves E, Parbrook P J and Martin R W 2014 Structural and optical properties of Ga auto-incorporated InAlN epilayers *Journal of Crystal Growth* **408** 97–101
- [29] Horcas I, Fernández R, Gómez-Rodríguez J M, Colchero J, Gómez-Herrero J and Baro a. M 2007 WSXM: A software for scanning probe microscopy and a tool for nanotechnology *Review of Scientific Instruments* **78** 13705
- [30] Vegard L 1921 Die Konstitution der Mischkristalle und die Raumfüllung der Atome - *Zeitschrift für Physik* **5** 17–26
- [31] Vurgaftman I and Meyer J R 2003 Band parameters for nitrogen-containing semiconductors *Journal of Applied Physics* **94** 3675–96
- [32] Terashima W, Che S B, Ishitani Y and Yoshikawa A 2006 Growth and characterization of AlInN ternary alloys in whole composition range and fabrication of InN/AlInN multiple quantum wells by RF molecular beam epitaxy *Japanese Journal of Applied Physics* **45** L539–42
- [33] Monteagudo-Lerma L, Valdueza-Felip S, Núñez-Cascajero A, González-Herráez M, Monroy E and Naranjo F B 2013 Two-step method for the deposition of AlN by radio frequency sputtering *Thin Solid Films* **545** 149–53
- [34] Guo Q, Shingai N, Nishio M and Ogawa H 1998 Deposition of InN thin films by radio frequency magnetron sputtering *Journal of Crystal Growth* **189–190** 466–70

- [35] Valdueza-Felip S, Naranjo F B, González-Herráez M, Lahourcade L, Monroy E and Fernández S 2011 High-surface-quality nanocrystalline InN layers deposited on GaN templates by RF sputtering *Physica Status Solidi (A)* **208** 65–9
- [36] Li J, Oder T N, Nakarmi M L, Lin J Y, Jiang H X and Al M 2002 Optical and electrical properties of Mg-doped p-type $\text{Al}_x\text{Ga}_{1-x}\text{N}$ *Applied Physics Letters* **80** 1210–2
- [37] Petrov I, Barna P B, Hultman L and Greene J E 2003 Microstructural evolution during film growth *Journal of Vacuum Science & Technology A: Vacuum, Surfaces, and Films* **21** S117
- [38] Liu H F, Tan C C, Dalapati G K and Chi D Z 2012 Magnetron-sputter deposition of high-indium-content n- AlInN thin film on p-Si(001) substrate for photovoltaic applications *Journal of Applied Physics* **112** 63114
- [39] Martin R W, Middleton P G, Donnell K P O and Stricht W Van Der 1999 Exciton localization and the Stokes' shift in InGaN epilayers *Applied Physics Letters* **74** 263
- [40] Pu X D, Shen W Z, Zhang Z Q, Ogawa H and Guo Q X 2006 Growth and depth dependence of visible luminescence in wurtzite InN epilayers *Applied Physics Letters* **88** 151904
- [41] Leroux M, Grandjean N, Beaumont B, Nataf G, Semond F, Massies J and Gibart P 1999 Temperature quenching of photoluminescence intensities in undoped and doped GaN *Journal of Applied Physics* **86** 3721–8
- [42] Varshni Y P 1967 Temperature dependence of the energy gap in semiconductors *Physica* **34** 149–54